RSC Advances

PAPER

View Article Online
View Journal | View Issue

Cite this: *RSC Adv.*, 2026, **16**, 22080

One-pot encapsulation of penicillin G into ZIF-8 and its antibacterial activity

Hani Nasser Abdelhamid *[a] and Ghada Abd-Elmonsef Mahmoud *[b]

Metal–organic frameworks (MOFs) provide adaptable platforms for drug delivery and antibacterial applications owing to their adjustable porosity, high surface area, and catalytic characteristics. We present the environmentally friendly, room-temperature synthesis of ZIF-8 nanocomposites, both with and without penicillin G encapsulation. The materials were comprehensively evaluated using XRD, Raman spectroscopy, FT-IR, DRS, SEM, and nitrogen sorption isotherms. Structural investigation verified high crystallinity, preservation of framework integrity upon drug encapsulation, and enabled the formation of hierarchical porosity with interparticle mesopores. SEM images identified nanoscale particles (50–100 nm), whereas DRS spectra showed a blue shift following drug encapsulation, suggesting an interaction between penicillin G and the ZIF-8 framework. The antibacterial assessment against Gram-positive (*Bacillus cereus*, *Staphylococcus aureus*) and Gram-negative (*Escherichia coli*, *Klebsiella pneumoniae*, *Pseudomonas aeruginosa*) bacteria revealed superior efficacy of penicillin-loaded ZIF-8 (ZIF3), resulting in decreasing CFU counts and lower MIC values relative to free penicillin and chloramphenicol (positive control antibiotic). These findings support the promise of ZIF-8-based nanocomposites as effective antibacterial agents for applications in wound healing, drug delivery, and public health protection.

Received 6th March 2026
Accepted 16th April 2026

DOI: 10.1039/d6ra01931e

rsc.li/rsc-advances

Introduction

Bacterial infections provide significant health risks and constitute a major global concern. The World Health Organization (WHO) unveiled the 2024 WHO Bacterial Priority Pathogens List (WHO BPPL) as a strategic instrument to address antibiotic resistance (AMR).[1] The 2024 WHO BPPL comprises 24 pathogens from 15 families of antibiotic-resistant bacteria. Their presence signifies both the substantial global burden of illness and issues related to transmissibility, limited treatment options, preventive challenges, emerging resistance patterns, and deficiencies in the research and development pipeline. The clinical efficacy of existing medicines varies significantly among countries and regions due to considerable differences in resistance rates and underlying mechanisms, shaped by economic and environmental factors. This heterogeneity influences the social value of antibiotics, many of which remain vulnerable to cross-resistance.[2,3] Antibacterial surfaces have emerged as effective techniques to address biofilm-associated infections through active, passive, and hybrid mechanisms, consequently enhancing the efficacy of biomedical materials.[4] Numerous antibacterial agents have been examined, including enzymes,[5] polysaccharides,[6,7] carbon dots,[8,9] Ti_3C_2/g-C_3N_4 composites,[10] essential oils,[11] and flavonoids.[12] Moreover, advanced materials have enabled the development of intelligent, stimuli-responsive platforms for antibacterial therapy.[13] Notwithstanding these advancements, the presence of significant challenges led to significant research efforts.[14] Consequently, ongoing research into advanced and multifunctional materials is crucial for developing more effective and sustainable antibacterial treatments.[15,16]

Metal–organic frameworks (MOFs) are hybrid porous materials with considerable potential for biomedical applications, including disease diagnostics and therapy.[17–20] They have been coupled with drugs,[21–24] MXenes,[25] and covalent organic frameworks (COFs)[26] to improve their functional efficacy. Due to their extensive surface area and adjustable porosity, MOFs have exceptional drug-loading capability.[27,28] Their toxicity is significantly affected by physicochemical parameters, including composition, particle size and shape, surface properties, biodegradability, and structural stability.[29–32] Recent advancements have focused on overcoming these limitations, minimizing toxicity, and enhancing therapeutic efficacy. Future research must include comprehensive toxicity evaluations and the development of innovative, optimized MOF composites to guarantee safety and therapeutic efficacy.[29–31] In addition to their medicinal potential, MOFs exhibit significant antimicrobial properties. There is a growing focus on synergistic approaches that enable targeted and effective antibacterial action while minimizing harm to healthy host cells. A sevenfold reduction in bacterial load has been accomplished *via* the

[a]*Department of Chemistry, College of Science, Imam Mohammad Ibn Saud Islamic University (IMSIU), Riyadh 11623, Saudi Arabia. E-mail: hnabdelhamid@imamu.edu.sa*

[b]*Botany and Microbiology Department, Faculty of Science, Assiut University, 71516, Assiut, Egypt. E-mail: ghadamoukabel@aun.edu.eg*

formation of intracellular reactive oxygen species (ROS), coupled with unobstructed water penetration and superior antifouling efficacy.[33] Additionally, membranes containing MOFs have demonstrated over 97.5% efficacy in removing divalent and monovalent salts and exceeding 95% removal of heavy metals, highlighting their significant potential for water remediation applications.[33] The antibacterial activity of MOFs can be enhanced by conjugation with other nanomaterials, such as gold nanoparticles (Au NPs)[34] and silver nanoparticles.[35,36] Moreover, MOFs can be incorporated into membrane systems, offering not only robust antibacterial properties but also significant benefits in water treatment.[37]

MOFs can encapsulate various molecules for various applications. Reports indicate its encapsulation of nanocatalysts,[38] metal nanoparticles,[39] single-molecule magnets,[40] fullerenes,[41] carbon dots,[42] phosphorus- and nitrogen-containing ionic liquids,[43] enzymes,[44,45] large biopolymers,[46] and diverse small molecules.[47–49] These host@MOF systems integrate the structural benefits of MOFs as host matrices with the functional characteristics of the encapsulated species, yielding synergistic guest@host@MOF architectures. These hybrid materials have exhibited notable efficacy in various applications.[50] A MOF-platform with dual targeting was developed to address intestinal infections caused by *Escherichia coli* (*E. coli*).[51] This dual-targeting antimicrobial strategy, which combines probiotic biofilms with *E. coli*-specific administration, represents a potential and safe therapeutic approach for restoring intestinal homeostasis in both human and animal healthcare.[51] Zirconium-based MOFs have also been examined for the encapsulation and controlled release of ciprofloxacin; however, the study did not assess antibacterial activity.[52]

This paper presents a sustainable and efficient one-pot method for encapsulating an antibiotic, *i.e.*, penicillin G, within an MOF under ambient conditions, utilizing water as an eco-friendly solvent. The drug was integrated into a zeolitic imidazolate framework (ZIF-8) *via* a simple synthetic method, underscoring the potential of MOFs as effective transporters for medicinal compounds. The characterization of the resultant materials was performed utilizing X-ray diffraction (XRD), Fourier-transform infrared spectroscopy (FT-IR), Raman spectroscopy, scanning electron microscopy (SEM), diffuse reflectance spectroscopy (DRS), and nitrogen adsorption–desorption analysis to verify structural integrity, encapsulation, and textural properties. The antibacterial efficacy of the drug-encapsulated framework was systematically assessed and compared with that of the unmodified framework and the free drug, serving as controls. The materials were evaluated against a panel of representative Gram-positive and Gram-negative pathogenic bacteria, exhibiting improved antibacterial efficacy. The novelty of this work lies in the first use of penicillin G as a structure-directing agent during the synthesis of ZIF-8, enabling a green, room-temperature preparation route. The novelty of this study lies in the encapsulation of penicillin G within an MOF structure, resulting in a nanocomposite characterized by hierarchical porosity and maintained framework integrity. The encapsulation technique markedly improves the antibacterial efficacy of penicillin G relative to the free antibiotic, owing to regulated, prolonged release from the ZIF-8 matrix and enhanced contact with bacterial cells. This method illustrates a new way to directly incorporate antibiotics into MOF synthesis, which may be further developed for scalable antibacterial nanomaterials and batch technologies in biomedical and public health applications. These findings highlight the potential of MOF-based drug delivery systems for enhanced antibacterial applications and necessitate additional comprehensive exploration.

Materials

Zinc nitrate hexahydrate ($Zn(NO_3)_2 \cdot 6H_2O$), 2-methylimidazole (Hmim), penicillin G potassium salt (benzylpenicillin potassium salt, PEN), and sodium hydroxide (NaOH) were obtained from Sigma-Aldrich (Germany). All chemicals were of analytical grade and used as received without further purification. Deionized water was used as the solvent throughout the experiments.

Synthesis of ZIF-8 and penicillin G-encapsulated ZIF-8

ZIF-8 materials, with and without drug loading, were synthesized using a similar procedure.[53] Briefly, 0.2 mL of NaOH solution (0.100 M) was added to 1.6 mL of zinc nitrate solution (0.84 M, 1.3 mmol). Subsequently, Hmim solution (16 mL, 3.00 M, 48 mmol) was introduced, and the total reaction volume was adjusted to 50 mL with deionized water before stirring at room temperature for 1 hour. The resulting solid product was collected by centrifugation (13 500 rpm for 10 minutes), washed twice with ethanol (2 × 20 mL) to remove unreacted species, and dried overnight in an oven at 85 °C. The drug-free material was designated as ZIF.

For drug-loaded samples, penicillin G was added to the zinc precursor solution before Hmim was added. Different drug-to-metal weight ratios (Zn^{2+} : penicillin G = 1 : 0.5, 1 : 1, and 1 : 2) were employed to investigate the effect of drug content on encapsulation efficiency and material properties. The corresponding products were labeled as ZIF1, ZIF2, and ZIF3, respectively.

The drug encapsulation efficiency was evaluated based on a UV-Vis spectrophotometer (Cary Eclipse 20) by measuring the absorbance at 322 nm.[54]

$$\text{The drug encapsulation efficiency } (\%) = \left(1 - \frac{A_{\text{free}}}{A_{\text{total}}}\right) \times 100$$

A_{total} denotes the absorbance of the initial drug solution before encapsulation, whereas A_{free} signifies the absorbance of the supernatant containing free (unencapsulated) medication following separation.

Characterization

XRD analyses were carried out using a PANalytical X'Pert Pro diffractometer (Cu Kα1 radiation). Surface morphology was further examined by SEM using a JEOL JSM-7000F instrument at accelerating voltages of 5.0 and 15.0 kV. Nitrogen adsorption–

desorption isotherms at 77 K and carbon dioxide adsorption isotherms at 298 K were obtained using a Micromeritics ASAP 2020 surface area analyzer. Prior to analysis, samples were degassed under vacuum at 110 °C for 3 hours. Total pore volumes were determined from nitrogen isotherms at a relative pressure (P/P_0) of 0.98. Pore size distributions were calculated using BJH adsorption dV/dlog(D) pore volume (Harkins and Jura: Faas Correction). DRS spectra were recorded with UV-2600i (SHIMADZU, Japan). FT-IR spectra were collected on an IRTracer-100 (SHIMADZU, Japan) over the wavenumber range of 4000–390 cm^{-1}. Raman spectra were collected using Ram II connected to FTIR Vertex 70 (Bruker).

Antibacterial activity

The antibacterial efficacy of five penicillin-based formulations (PEN, ZIF, ZIF1, ZIF2, and ZIF3) was evaluated against five foodborne pathogenic bacteria. The bacterial isolates were cultured and maintained on nutrient agar (NA) medium.[55,56]

Bacterial inocula were prepared by growing each strain in nutrient broth containing beef extract (1%), peptone (1%), and NaCl (0.5%), in 100 mL of distilled water (initial pH 6.8). Cultures were incubated at 30 °C for 24 hours under shaking conditions (200 rpm). The cells were harvested by centrifugation at 6000×g for 10 minutes, washed twice with sterile saline solution, and resuspended to obtain a final concentration of approximately 10^5 colony-forming units per milliliter (CFU mL^{-1}).

For antibacterial testing, 50 μg mL^{-1} of each penicillin derivative was added to 10 mL of sterile nutrient broth. Chloramphenicol (CHL) was used as a positive control, while broth without any antimicrobial agent served as a negative control. Each tube was inoculated with 1% (v/v) of the standardized bacterial suspension and incubated at 30 °C for 48 hours.

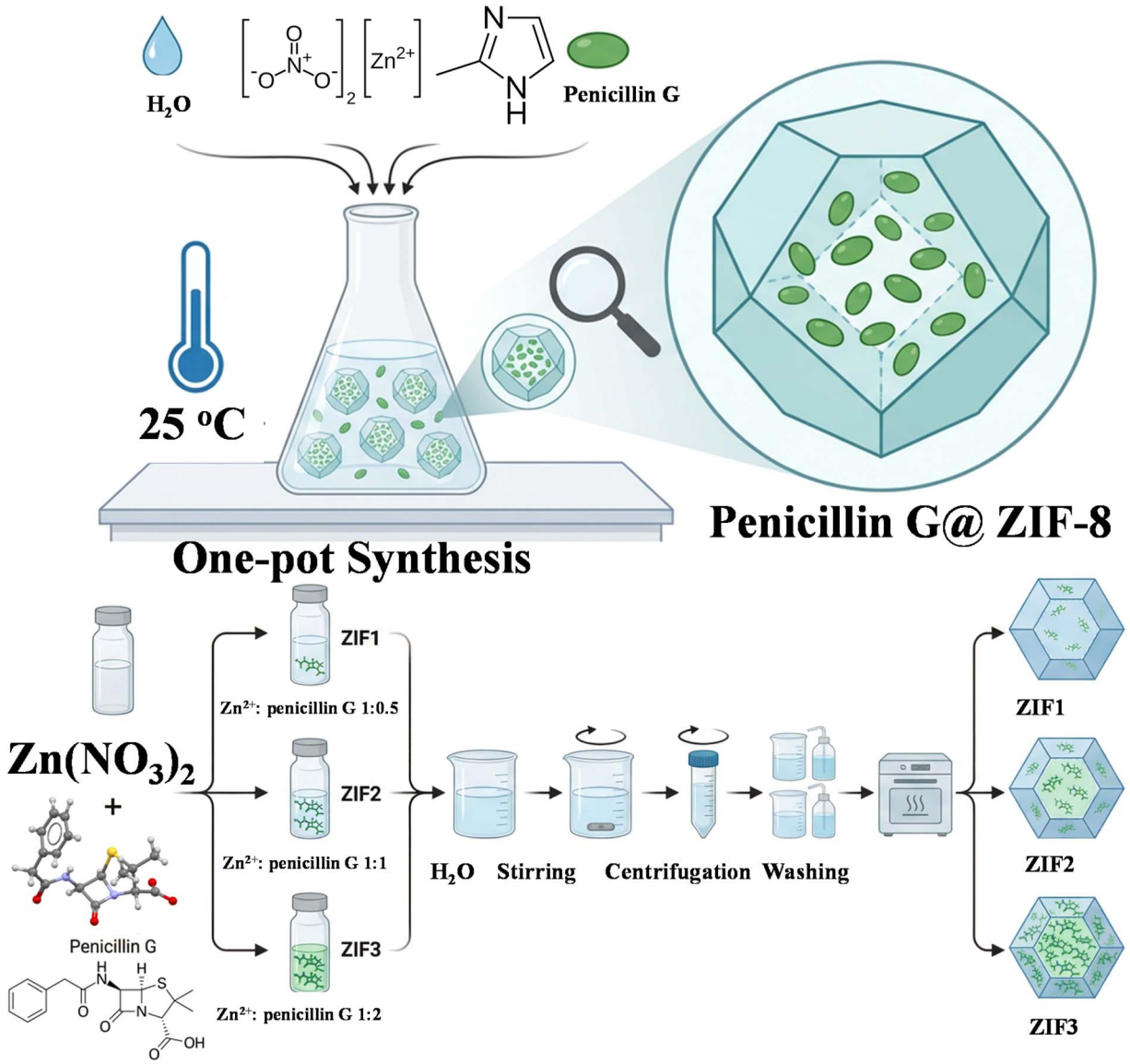

Fig. 1 Synthesis and encapsulation procedure for ZIF-8 with and without penicillin G. The upper part shows the principle of the synthesis, while the part below shows the drug encapsulation with different ratios.

Bacterial growth was monitored by measuring the optical density at 660 nm (OD_{660}), and viable counts were determined by calculating colony-forming units per milliliter (CFU mL^{-1}).[57]

The minimum inhibitory concentration (MIC) of each formulation was determined according to a standard broth dilution method.[58] Serial concentrations ranging from 0 to 25 μg mL^{-1} were prepared in nutrient broth and inoculated with approximately 10^5 CFU mL^{-1} of each bacterial strain. After incubation at 30 °C for 48 hours, the MIC was defined as the lowest concentration that inhibited visible bacterial growth, confirmed by CFU enumeration. Bacterial data were presented as the mean of replicates ± the standard deviation (SD). The significant variations between treatments were detected using one-way analysis of variance at <0.05 (*p*-value).

Results and discussion

Materials synthesis and characterization

Fig. 1 shows the synthesis procedure for ZIF-8, both with and without penicillin G. ZIF-8 materials, both unmodified and drug-encapsulated, were produced by a simple aqueous method under ambient conditions (Fig. 1). In a standard protocol, the zinc precursor was initially treated with a moderate base to initiate the synthesis of intermediate zinc hydroxynitrate nanosheets, which provide interlayer gaps (9.8 Å, approx. 1 nm) that accommodate guest molecules, *i.e.*, penicillin G.[59–61] Thereafter, the organic linker (2-methylimidazole) was included to facilitate framework formation, resulting in the crystallization of ZIF-8. The resultant powders were isolated, washed to remove unreacted substances, and dried to obtain the final products. In drug-encapsulated samples, penicillin G was incorporated into the reaction mixture before the linker was added, facilitating the antibiotic's incorporation into the intermediate layered structure preparatory to framework assembly and encapsulation. Various drug-to-Zn ratios were utilized to examine the effect of drug presence on material characteristics. The drug-free material was designated as ZIF, whereas the drug-loaded samples were classified as ZIF1, ZIF2, and ZIF3 based on ascending drug content (Fig. 1). The materials were characterized using XRD (Fig. 2a), Raman spectra (Fig. 2b), FT-IR (Fig. 3a), DRS (Fig. 3b), SEM images (Fig. 4), and nitrogen sorption isotherms (Fig. 5).

The XRD patterns of ZIF-8, both before and following penicillin G encapsulation (Fig. 2a), demonstrate the establishment of the intended crystalline framework. The measured diffraction patterns closely align with the simulated pattern for ZIF-8, thereby validating the formation of the desired sodalite-type structure. The absence of extra diffraction peaks indicates that no secondary crystalline phases or impurities were generated during synthesis, thereby confirming the high phase purity of the synthesized materials. The strong, well-defined diffraction peaks further indicate the high crystallinity of both the

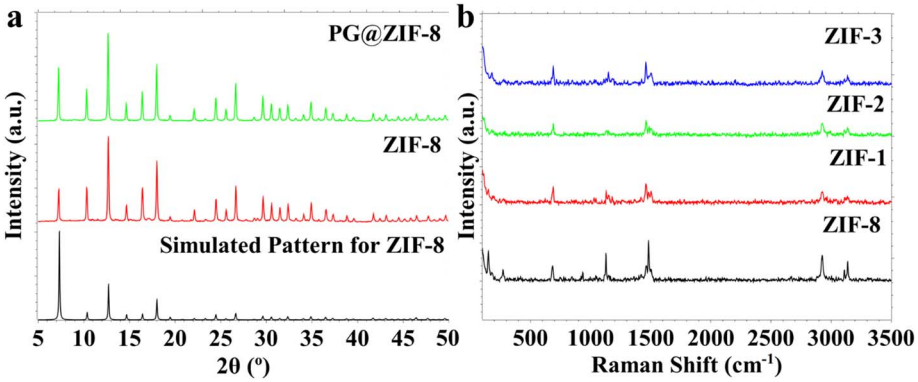

Fig. 2 Characterization of the materials using (a) XRD, and (b) Raman spectra.

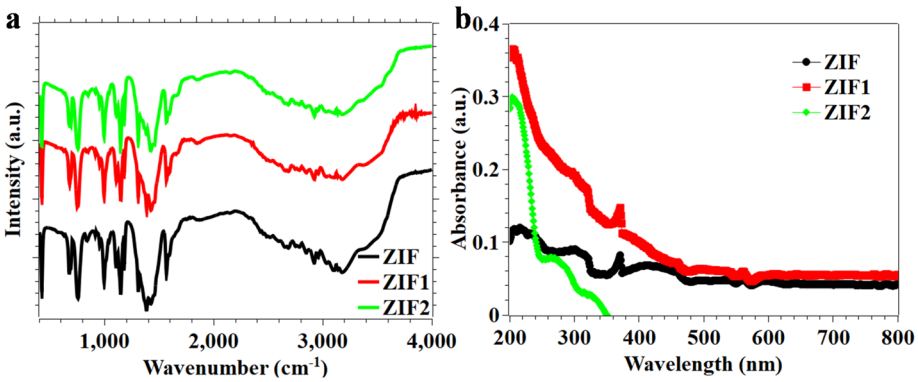

Fig. 3 (a) FT-IR, and (b) DRS spectra for the synthesized materials.

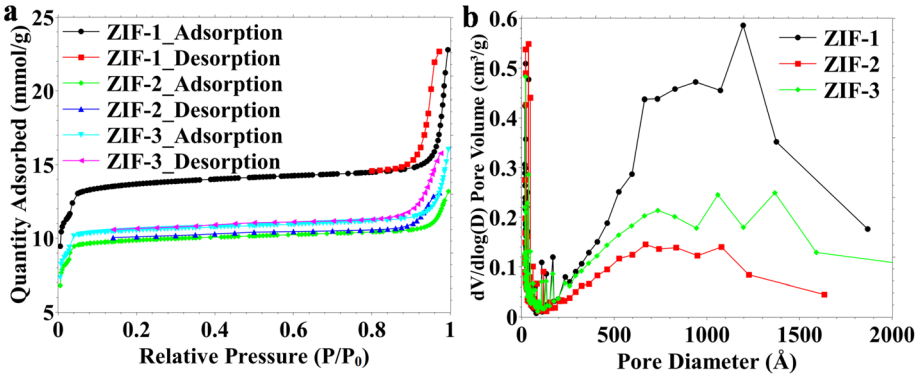

Fig. 4 (a) Nitrogen adsorption/desorption isotherms and (b) BJH pore size distribution.

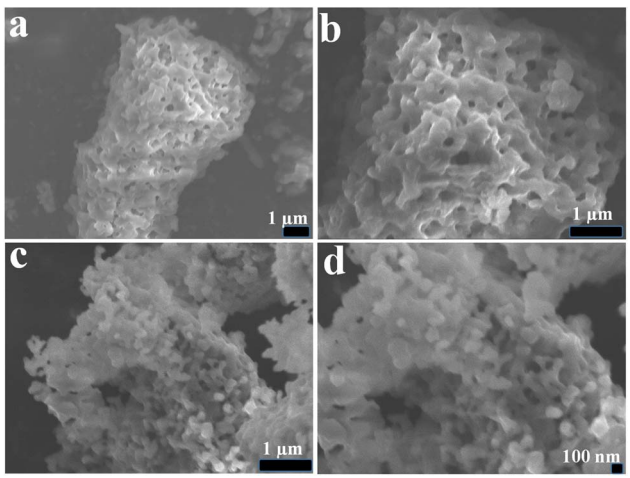

Fig. 5 SEM images of (a and b) ZIF1 and (c and d) ZIF3 at different magnifications.

virgin and drug-loaded samples. Distinct reflections identified at Bragg angles (2θ) of roughly 7.2°, 10.3°, 12.6°, 14.7°, 16.5°, 18.2°, 19.4°, 21.9°, 24.6°, 25.9°, 26.7°, 29.9°, 30.6°, 32.5°, 32.9°, and 34.8° align with the standard crystallographic planes of ZIF-8 (Fig. 2a). The observed peaks align with previously published data for ZIF-8, validating the successful assembly of zinc nodes with Hmim linkers. The XRD patterns of the penicillin G-loaded samples retain the primary diffraction characteristics of pristine ZIF-8, indicating that the framework structure remains unaltered upon drug incorporation. The maintenance of peak positions indicates that encapsulation occurs without significant structural distortion or collapse of the crystalline lattice. Occasionally, tiny fluctuations in peak intensity or modest broadening may occur, either to guest molecules within the pores or to subtle alterations in crystal size and lattice strain caused by drug inclusion. The XRD analysis verifies that the one-pot encapsulation method preserves the structural integrity and crystallinity of ZIF-8, affirming its efficacy as a reliable carrier for antibiotic loading (Fig. 2a).

The structural connectivity and chemical integrity of the synthesized materials were further examined using Raman (Fig. 2b) and FT-IR (Fig. 3a) spectroscopy. The Raman spectra of pristine ZIF-8 and penicillin G-loaded samples (ZIF1, ZIF2, and ZIF3) exhibit analogous spectral bands, indicating that the essential framework structure is maintained post-drug encapsulation (Fig. 2b). The unaltered ZIF-8 exhibits more pronounced, sharper Raman bands than the drug-loaded variants, indicating a minor decrease in crystallinity or heightened structural disorder arising from the inclusion of penicillin G in the pores. The Raman bands detected at low wavenumbers, around 141 and 153 cm^{-1}, are attributed to lattice vibrations and Zn–N stretching modes associated with the coordination of Zn^{2+} centers to imidazolate linkers (Fig. 2b). The band at roughly 683 cm^{-1} corresponds to in-plane bending vibrations of the imidazole ring, whereas the feature near 1119 cm^{-1} is attributed to C–N stretching modes of the linker. The band at 1475 cm^{-1} mostly corresponds to C=N stretching vibrations of the imidazolate ring, while the high-frequency bands at 2930 and 3134 cm^{-1} are assigned to aliphatic and aromatic C–H stretching vibrations, respectively. Significantly, variations in intensity and minor broadening of the bands at 1475 and 3134 cm^{-1} in the drug-loaded samples indicate interactions between the functional groups of penicillin G and the ZIF-8 framework, implying encapsulation within the porous structure rather than mere surface adsorption.

The FT-IR spectra of both pristine and penicillin G-loaded ZIF-8 samples have analogous characteristic absorption bands, hence affirming the retention of the framework structure (Fig. 3a). The band at around 423 cm^{-1} is attributed to Zn–N stretching vibrations, thereby confirming the formation of coordination bonds between zinc ions and imidazolate linkers. The peak at 667 cm^{-1} belongs to bending vibrations of the imidazole ring, whereas the band at 752 cm^{-1} pertains to out-of-plane bending of the imidazole ring. The absorption at 991 cm^{-1} is ascribed to C–N stretching, while the band at 1143 cm^{-1} is associated with in-plane ring vibrations. The peaks at 1308 and 1412 cm^{-1} for C–N and C=N, respectively, while the band at 1571 cm^{-1} is attributed to aromatic C=N stretching within the imidazolate framework. The retention of these distinctive Zn–N and imidazolate-associated bands following drug insertion signifies that the crystalline framework is structurally unchanged. No additional bands indicative of distinct crystalline phases are seen, demonstrating that the encapsulation of penicillin G does not interfere with framework

development. The changes in band intensity and sharpness indicate effective drug incorporation within the pores, while preserving the overall connectivity and integrity of the ZIF-8 structure (Fig. 3a).

The optical characteristics of the synthesized materials were analyzed *via* DRS, as seen in Fig. 3b. The untainted ZIF-8 sample has a pronounced absorption band in the UV spectrum, peaking at approximately 214 nm (Fig. 3b). The absorption is due to ligand-centered $\pi \rightarrow \pi^*$ transitions in the 2-methylimidazolate linker. The band location aligns with the broad band gap characteristics of ZIF-8, affirming its inherent UV-responsive properties (Fig. 3b). Encapsulation of penicillin G significantly alters the absorption profile. The drug-loaded samples (ZIF1, ZIF2, and ZIF3) exhibit a minor blue shift of the principal absorption band to around 205 nm (Fig. 3b). This alteration indicates changes in the local electrical environment of the framework, probably resulting from interactions between the functional groups of penicillin G (including amide, carboxylate, and aromatic moieties) and the internal surface of ZIF-8. Such interactions may affect the electron-density distribution within the framework, thereby altering the electronic transition energy. The spectral shift and changes in absorption intensity further validate the integration of penicillin G within the porous structure. The absence of new broad absorption features in the visible range indicates that the underlying electronic structure of ZIF-8 is largely preserved post-encapsulation. The DRS results affirm the structural integrity of the framework and indicate that penicillin G loading generates changes in the material's optical characteristics.

The porosity and textural characteristics of the synthesized materials were assessed by nitrogen adsorption–desorption isotherms at 77 K (Fig. 4a), with the associated pore size distributions illustrated in Fig. 4b. Table 1 summarizes the calculated surface areas, pore volumes, and pore size characteristics obtained from several analytical models. Pristine ZIF-8 has a classic type I isotherm typical of microporous materials, indicating its well-defined pore structure and elevated surface area. The high micropore surface area (1345 $m^2\ g^{-1}$) and constrained micropore volume (0.575 $cm^3\ g^{-1}$), determined *via* the Dubinin–Astakhov model, affirm the preeminence of microporosity. The BET surface area of ZIF-8 is 886 $m^2\ g^{-1}$, the Langmuir surface area is considerably greater at 1608 $m^2\ g^{-1}$, aligning with the extensive internal surface characteristic of its sodalite-type structure. The *t*-plot analysis corroborates its primarily microporous characteristics, revealing a micropore area of 739 $m^2\ g^{-1}$ and external surface area of 146 $m^2\ g^{-1}$. Following the encapsulation of penicillin G (ZIF1, ZIF2, and ZIF3), a significant decrease in surface area and pore volume is observed. The BET surface areas diminish to 635 $m^2\ g^{-1}$ for ZIF2 and 679 $m^2\ g^{-1}$ for ZIF3, while the micropore volumes, ascertained *via* the *t*-plot approach, reduce to 0.306 $cm^3\ g^{-1}$ and 0.331 $cm^3\ g^{-1}$, respectively. The decrease is attributed to partial colonization of micropores by penicillin molecules, which restricts nitrogen availability within the interior cavities. The limiting micropore volume decreases from 0.575 $cm^3\ g^{-1}$ in ZIF to 0.482–0.502 $cm^3\ g^{-1}$ in the drug-loaded samples, thereby indicating the successful integration of the antibiotic inside the framework.

Pore size studies using BJH and Dollimore–Heal (D–H) methodologies reveal further mesoporous contributions following drug encapsulation (Fig. 4b). The average pore widths for adsorption and desorption exhibit a small increase (*e.g.*, the

Table 1 Textural analysis of values extracted from nitrogen sorption isotherm

	Materials		
Parameters	ZIF-1	ZIF-2	ZIF-3
Dubinin-Astakhov			
Micropore surface area ($m^2\ g^{-1}$)	1345	1028	1089
Limiting micropore volume ($cm^3\ g^{-1}$)	0.575	0.482	0.502
Surface area (m^2g^{-1})			
Single point surface area at $p/p^\circ = 0.300290916$ ($m^2\ g^{-1}$)	947	681	727
BET surface area ($m^2\ g^{-1}$)	886	635	679
Langmuir surface area ($m^2\ g^{-1}$)	1608	1101	1225
t-Plot micropore area ($m^2\ g^{-1}$)	739	554	599
t-Plot external surface area ($m^2\ g^{-1}$)	146	80	79
BJH adsorption cumulative surface area of pores ($m^2\ g^{-1}$)	1243	65	65
Single-point adsorption total pore volume of pores less than 1255.755 Å diameter at $p/p^\circ = 0.984482264$ ($cm^3\ g^{-1}$)	0.705	0.435	0.502
***t*-Plot micropore volume** ($cm^3\ g^{-1}$)	0.410	0.306	0.331
Pore size adsorption average pore width ($4V/A$ by BET, Å)	31	27	29
Dubinin–Astakhov			
Micropore surface area ($m^2\ g^{-1}$)	1345	1028	1089
Limiting micropore volume ($cm^3\ g^{-1}$)	0.575	0.482	0.502
MP-method			
Cumulative surface area of pores between 2.6362 Å and 19.6000 Å hydraulic radius ($m^2\ g^{-1}$)	1255	969	1047

adsorption average pore width rises from 31 Å in ZIF to 27–29 Å in drug-loaded samples, accompanied by broader distributions extending into bigger pore sizes). The data indicate the formation of hierarchical porosity, perhaps resulting from interparticle voids, partial pore obstruction, or structural reconfigurations during drug integration. The cumulative surface area and pore volume values obtained from the BJH and D–H models indicate diminished mesoporous surface contributions in drug-loaded samples relative to pure ZIF-8, potentially reflecting variations in aggregation or packing density post-encapsulation (Fig. 4b). Moreover, the Freundlich and Dubinin–Astakhov parameters indicate a reduced adsorption capacity ($Qm \times C$ values) in drug-loaded materials, consistent with pore-filling effects. Nitrogen sorption studies indicate that pure ZIF-8 is a highly microporous material with a substantial surface area and pore volume. Encapsulation of penicillin G results in partial pore occupation, thereby decreasing microporosity and surface area while facilitating the development of hierarchical pore structures. These modifications significantly facilitate effective drug loading within the porous framework while preserving structural integrity and accessible porosity.

The morphology and particle size of the produced materials were analyzed using SEM, as illustrated in Fig. 5 for ZIF1 and ZIF3. The SEM images demonstrate the creation of nanoscale particles with reasonably uniform shape and high dispersion. The estimated particle size ranges from roughly 50 to 100 nm, indicating the formation of nanocrystalline ZIF-8 structures despite drug encapsulation. The particles manifest as aggregated nanocrystals, creating clusters with voids (interparticle porosity). The interparticle voids facilitate the formation of mesoporosity, aligning with the hierarchical pore attributes identified through nitrogen sorption studies. The presence of interparticle mesopores may enhance mass transfer and promote the diffusion of guest molecules, which is beneficial for drug-release applications. Crucially, no notable morphological collapse or structural deformation is seen following the integration of penicillin G, affirming that the encapsulation process retains the overall particle morphology while preserving nanoscale dimensions.

The one-pot synthesis of penicillin G-loaded ZIF-8 under ambient, aqueous conditions presents significant benefits over traditional MOF synthesis methods, including solvothermal or multi-step post-loading techniques. Conventional solvothermal methods typically require organic solvents, high temperatures, and extended reaction times, increasing costs, energy use, and environmental impacts. Moreover, such severe temperatures are inappropriate for thermally and chemically sensitive antibiotics. Penicillin G exhibits excellent stability in aqueous environments at a pH range of 5.0–8.0, particularly near neutral pH (~7), but it rapidly degrades in severely acidic or basic conditions and at high temperatures due to the cleavage of the β-lactam ring.[62] Its stability markedly decreases with rising temperature; it can maintain stability for extended periods when preserved under mild conditions (*e.g.*, in chilled aqueous solutions) or in the presence of polymer materials.[63] Even green solvents such as ionic liquids show limitations for the use of penicillin G.[64] For example, the stability of Penicillin G in the ionic liquid 1-butyl-3-methylimidazolium hexafluorophosphate ([Bmim]PF_6) is significantly affected by pH and temperature, with enhanced stability as pH increases from 1.5 to 4.0 and temperature decreases. Under optimum conditions (pH 2.0 and 10 °C), penicillin G demonstrates a half-life of around 17.7 hours, according to first-order kinetics, with three rearranged isomers identified at pH 2.0, whose structures remain invariant with temperature changes.[64] Thus, the ideal circumstances for preserving the stability of Penicillin G sodium require a citrate buffer solution with a buffer-to-penicillin molar ratio of at least 0.75, at roughly pH 7.0.[65] The temperature must be kept at or below 25 °C to reduce degradation and retain the integrity of the antibiotic. The moderate, room-temperature, water-based synthesis employed in this study offers a significant advantage by maintaining the chemical integrity of penicillin G during MOF formation and by circumventing conditions that could accelerate deterioration. The single-step procedure eliminates supplementary post-synthetic loading steps, thereby reducing processing time and solvent use and rendering the method more ecologically sustainable and possibly scalable for the future synthesis of antibacterial nanomaterials. This method offer also an encapsulation efficiency of 80–90%.

Antibacterial efficacy

The antibacterial efficacy of five penicillin formulations (PEN, ZIF, ZIF1, ZIF2, and ZIF3) at a concentration of 50 μg mL^{-1} was assessed against five human pathogenic bacteria: *Escherichia coli*, *Klebsiella pneumoniae*, *Pseudomonas aeruginosa*, *Bacillus cereus*, and *Staphylococcus aureus* (Fig. 6). The results were juxtaposed against Chloramphenicol (CHL), serving as the positive control, and untreated cultures, serving as the negative control. All penicillin-derived formulations exhibited significant antibacterial activity, whereas the control samples showed the highest viable bacterial numbers. ZIF3 exhibited the most

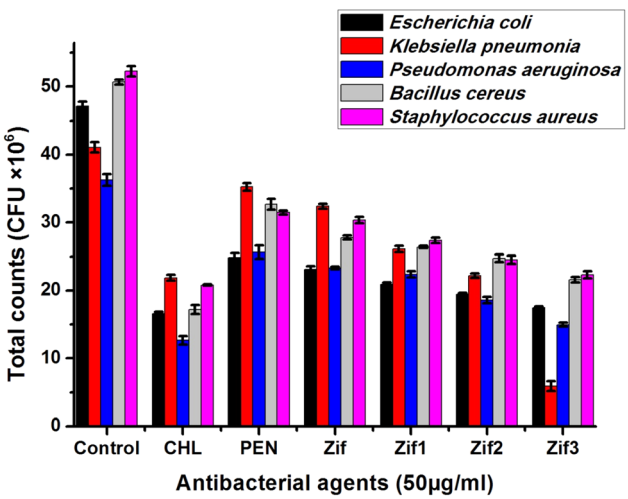

Fig. 6 The antibacterial activity of penicillin derivatives against five human pathogenic bacteria (*Escherichia coli*, *Klebsiella pneumoniae*, *Pseudomonas aeruginosa*, *Bacillus cereus*, and *Staphylococcus aureus*) was compared with that of chloramphenicol (CHL) as a standard antibacterial agent and free antibacterial medium (control). Data were expressed as mean ± SD, $p < 0.05$.

pronounced antibacterial activity among the evaluated materials, with significantly reduced CFU levels across all strains. ZIF3 diminished bacterial counts to 17.5×10^6 CFU mL^{-1} for *E. coli*, 5.92×10^6 CFU mL^{-1} for *K. pneumoniae*, 14.96×10^6 CFU mL^{-1} for *P. aeruginosa*, 21.6×10^6 CFU mL^{-1} for *B. cereus*, and 22.3×10^6 CFU mL^{-1} for *S. aureus*. The results are significantly lower than those achieved with free penicillin, suggesting improved antibacterial efficacy following encapsulation. Free penicillin (PEN) demonstrated modest antibacterial efficacy but was inferior to ZIF3, exhibiting high residual CFU values across all strains. Chloramphenicol exhibited robust antibacterial efficacy; however, ZIF3 displayed equivalent or, in some instances, enhanced inhibition against certain strains. The intermediate formulations (ZIF, ZIF1, and ZIF2) significantly diminished bacterial counts relative to controls, with enhanced efficacy noted as drug loading increased, indicating a dose-dependent improvement linked to encapsulation efficiency. The enhanced antibacterial efficacy of drug-loaded ZIF materials may be ascribed to multiple factors: (i) increased stability of penicillin within the porous matrix, (ii) sustained or regulated release characteristics, and (iii) increasing interaction between the nanostructured carrier and bacterial cell membranes. The nanoscale particle size (50–100 nm) and hierarchical porosity may further promote interaction with bacterial membranes, hence augmenting antibacterial efficacy.

The minimum inhibitory concentrations (MICs) of the five formulations were assessed across a concentration spectrum of 0–25 μg mL^{-1} (Fig. 7a–e). Bacterial growth inhibition generally increased with higher treatment concentrations, confirming a concentration-dependent antibacterial effect. The majority of isolates exhibited MICs between 5 and 10 μg mL^{-1}. ZIF-based formulations consistently demonstrated reduced MIC values (5 μg mL^{-1}) relative to free penicillin (10 μg mL^{-1} in multiple instances), signifying enhanced antibacterial efficacy post-encapsulation. ZIF, ZIF1, ZIF2, and ZIF3 exhibited MIC values of 5 μg mL^{-1} against *E. coli* and *K. pneumoniae*, whereas free penicillin necessitated 10 μg mL^{-1} for equivalent inhibition. Comparable trends were observed for *P. aeruginosa*, *B. cereus*, and *S. aureus*, in which the encapsulated formulations demonstrated effective suppression at lower or equivalent concentrations compared to PEN. The MIC results validate the CFU findings, demonstrating that encapsulation of the medication within the ZIF-8 framework enhances antibacterial activity. The uniform efficacy observed in both Gram-positive and Gram-negative pathogens underscores the extensive applicability of the formulated nanocomposite system. The findings indicate that ZIF-based delivery systems can enhance antibiotic efficacy, perhaps reducing required dosages and aiding efforts to tackle bacterial resistance.

The antibacterial efficacy of MOF-based systems is regulated by several mechanisms, including ROS formation, ion release, photocatalytic activity, and cascade catalytic events.[66–68] Several MOFs have been reported to exhibit artificial enzymatic activity, MOFZyme.[69,70] ZIF-8 exhibits enzymatic activity, specifically peroxidase activity,.[71] Ou *et al.* created a GOx@MIL-53(Fe)@PVP nanosystem wherein glucose is converted to H_2O_2 by *in situ* embedded GOx, which is subsequently converted into hydroxyl radicals *via* the peroxidase-like activity of MIL-53(Fe), resulting in bacterial kill rates of 99.7% and 99.8% against *S. aureus* and *Escherichia coli*, respectively, while facilitating rapid wound healing in infected murine models with minimal harm to healthy tissues.[72] Notwithstanding these encouraging outcomes, the synthesis of MIL-53(Fe) requires high hydrothermal temperatures and potentially hazardous chemicals that could diminish enzyme performance, while post-synthesis analysis indicated a comparatively modest GOx loading (5.9 wt%) primarily on the exterior surfaces. Zinc-imidazolate MOFs such as ZIF-8 demonstrate nearly complete inactivation of *E. coli* (>99.9999%) under simulated solar irradiation within 2 hours, as ligand-to-metal charge transfer (LMCT) processes produce photoelectrons at Zn^{2+} centers that facilitate ROS generation, underscoring their inherent photocatalytic antibacterial capabilities.[73] The integration of noble metals, specifically Au, into ZIF-8 (Au@ZIF-8) within injectable hydrogels amplifies ROS production under visible light (>400 nm) *via* surface plasmon resonance and Schottky junction effects, leading to significant antibacterial efficacy against *E. coli* and *S. aureus* and to expedited wound healing.[34] Pre-synthesized MOFs can be integrated into polymeric fibers through electrospinning, exemplified by MXene/ZIF-8/polylactic acid membranes, which exhibited antibacterial efficacy exceeding 99.8% against *E. coli* and MRSA under 808 nm irradiation; nevertheless, challenges persist, including diminished MOF crystallinity and restricted loading capacity.[74] The integration of metal nanoparticles within MOFs presents a viable strategy: polymer-based Cu-MOF nanosheets infused with Ag nanoparticles (polyCu-MOF@AgNPs) demonstrated significant Ag^+ release, regulated Cu^{2+} release, ROS-induced bacterial membrane disruption, and metabolic interference, resulting in increasing antibacterial efficacy both *in vitro* and *in vivo*, alongside enhanced wound healing characterized by substantial collagen deposition.[35] These studies collectively illustrate that MOF-based antibacterial systems can utilize ROS generation, catalytic reactions, photocatalysis, ion release, and structural interactions to attain broad-spectrum antibacterial efficacy. ZIF-8 offers advantages in structural stability, simplicity, and inherent photocatalytic activity, whereas enzyme-loaded Fe-MOFs and noble metal composites provide additional cascade or plasmon-enhanced functionalities.[34,35,73,74]

Table 2 presents a range of ZIF-based antibacterial compounds, detailing their compositions, manufacturing techniques, target bacteria, bioassays, efficiencies, and processes. Most published systems utilize metals (Ce, Zn, Cu, Ag), photosensitizers (Ce6), antibiotics (Rifaximin, CUR), or enzymes (CAT), functioning predominantly through ROS formation, metal ion release, or enzymatic activity, with efficiency varying from 65% to 100% against *S. aureus* and *E. coli* (Table 2).[75–80] This study presents the penicillin G@ZIF-8 nanocomposite, which exhibits exceptional broad-spectrum antibacterial efficacy (MIC 5 μg mL^{-1}) against both Gram-positive (*B. cereus*, *S. aureus*) and Gram-negative (*E. coli*, *K. pneumoniae*, *P. aeruginosa*) bacteria, through regulated antibiotic release rather than metal toxicity or reactive oxygen species. The one-pot, room-temperature aqueous synthesis offers a simple and environmentally friendly alternative to previously

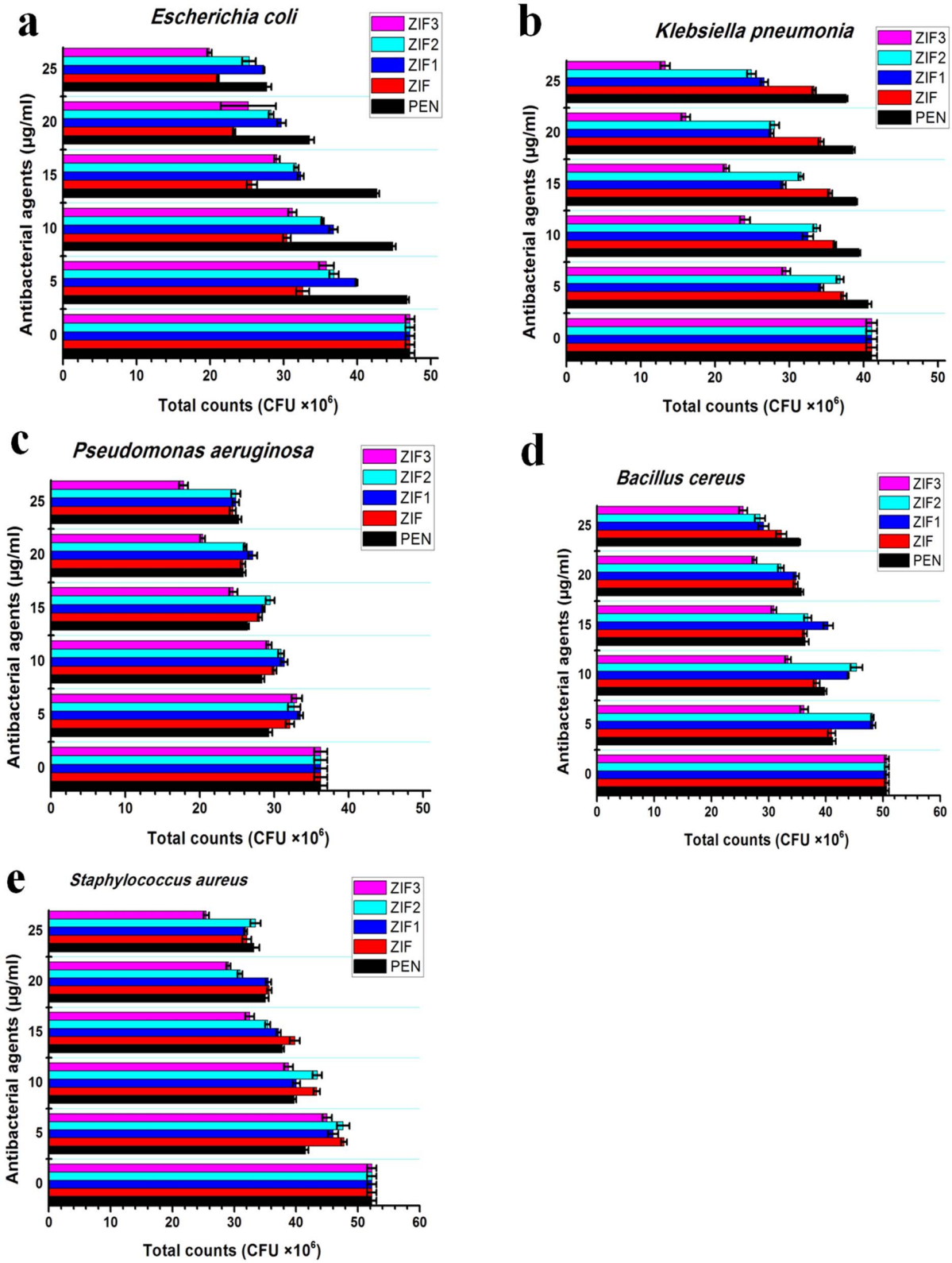

Fig. 7 (a–e): The minimal inhibiting concentration of penicillin derivatives against five human pathogenic bacteria (*Escherichia coli*, *Klebsiella pneumoniae*, *Pseudomonas aeruginosa*, *Bacillus cereus,* and *Staphylococcus aureus*) compared with free antibacterial medium (control). Data were expressed as mean ± SD, $p < 0.05$.

Table 2 Summary for ZIF-based antibacterial activity

MOFs	Compositions	Synthesis	Cells	Bio-assay	Efficiency	Mechanism	Ref.
Ce-ZIF-8@Ce6, Ce-ZIF-8@PDA, Ce-ZIF-8@PDA@Ce6, ZIF-8@PDA@Ce6	Ce Zn Hmim PDA Ce6	Heating with stirring at 50 °C for 1 hour Stirred at room temperature for 4 hours	*S. aureus*	MIC	200 μg mL^{-1} (ZIF-8) 100 μg mL^{-1} (Ce-ZIF-8)	ROS formation	75
ZIF-8@PDA	Zn Hmim PDA	Stirring and heating at 60 °C	*S. aureus*	ZOI CFU	99%	Zn^{2+} release	76
ZIF-L@Cotton	Zn Hmim	*In situ* growth method, stirring for 3h	*E. coli* *S. aureus*	ZOI	10.2 mm (*E. coli*) 11.2 mm (*S. aureus*)	Release Zn^{2+} ions	77
Cu@ZIF-L@Cotton	Cu Zn Hmim	Stirring for 3h Soaking for 3h (in Cu solution)	*E. coli* *S. aureus*		10.3 mm (*E. coli*) 12.9 mm (*S. aureus*)		
R-ZnO@ZIF-8	Zn ZnO Hmim Rifaximin	Stirring for 2 hours	*S. aureus*	CFU	80%	ROS formation	78
ZIF-8	Zn Hmim CUR	One-pot synthesis	*E. coli* *S. aureus*	CFU	>99%	Release of Zn^{2+} ions	79
CAT@ZIF-8/AgNPs	Zn Hmim AgNPs CAT	Microwave, 40 °C, 15 min	*E. coli*, *S. aureus*, *P. aeruginosa*	CFU	100%	Ag^{+} ions releaseEnzymatic activity	80
Pencillin G@ZIF-8	Zn Hmim Penicillin G	Room temperature One-pot method	*B. cereus*, *S. aureus* *Scherichia coli*, *K. pneumoniae*, *P. aeruginosa*	MIC	5 μg mL^{-1}	Penciling G release	This study

reported heating or multi-step techniques, underscoring its promise for scalable and biocompatible MOF-based antimicrobial applications (Table 2).[75–81] The material of penicillin G-loaded ZIF-8 can also be further suggested for other applications, such as sunblock creams offering UV protection and antibacterial activity.[82]

Conclusion

This study produced penicillin G-loaded ZIF-8 nanocomposites *via* a mild, eco-friendly approach at room temperature, using water as the solvent. Thorough characterization using XRD, Raman, FT-IR, SEM, TEM, DRS, and nitrogen sorption measurements verified that the crystalline structure of ZIF-8 was preserved during drug encapsulation. The materials displayed nanoscale particle dimensions (50–100 nm) and hierarchical porosity, conducive to effective drug loading and transport. DRS data demonstrated strong interactions between penicillin G and the ZIF-8 framework, whereas nitrogen sorption analysis indicated a change from exclusively microporous structures to hierarchical micro–mesoporous architectures, enabling regulated drug release. Antibacterial assessments revealed that penicillin-encapsulated ZIF-8, especially the ZIF3 variant, exhibited markedly enhanced efficacy against both Gram-positive and Gram-negative bacteria. The nanocomposite decreased colony-forming units and minimum inhibitory concentrations more efficiently than free penicillin and the reference antibiotic chloramphenicol. The superior antibacterial efficacy is due to the combined effects of reactive oxygen species production, nanoscale interactions with bacterial membranes, and enhanced drug diffusion facilitated by the porous ZIF-8 matrix. These findings underscore penicillin-loaded ZIF-8 as a promising nanoplatform for antibacterial therapy and possible wound-healing applications. Subsequent research should focus on *in vitro* and *in vivo* biocompatibility evaluations, comprehensive drug-release kinetics, and long-term stability and toxicity assessments. This method may also be applied to other antibiotics and MOF systems, facilitating the creation of scalable MOF-based antibacterial delivery platforms and sophisticated antimicrobial technologies for biomedical and public health purposes.

Conflicts of interest

The authors declear no conflict of interest.

Data availability

All data are presented in the manuscript. Raw data are available upon reasonable request from the authors.

References

1 WHO, *2024 WHO Bacterial Priority Pathogens List (WHO BPPL)*, 2024, https://www.who.int/news-room/fact-sheets/detail/antimicrobial-resistance.
2 M. J. Sweet, D. Ramnath, A. Singhal and R. Kapetanovic, *Nat. Rev. Immunol.*, 2025, **25**, 92–107.
3 U. Theuretzbacher, *Nat. Rev. Microbiol.*, 2025, **23**, 491–508.
4 Q. Su, Y. Xue, C. Wang, Q. Zhou, Y. Zhao, J. Su and B. Zhu, *Bioact. Mater.*, 2025, **53**, 114–140.
5 Z. Hu, H. Xu, Y. Ding, Q. Zhou, S. Feng, Y. Li, D. Di, S. Wang and Q. Zhao, *Coord. Chem. Rev.*, 2025, **543**, 216939.
6 M. He, Y. Huang, J. Wang, Z. Chen, J. Xie, Z. Cui, D. Xu, X. Zhang and W. Yao, *Int. J. Biol. Macromol.*, 2025, **308**, 142598.
7 J. Li, Y. Liu and X. Zhao, *Chem. Eng. J.*, 2025, **517**, 163776.
8 B. Wang, G. Zhou, Q. Shi, W. Fan and X. Xie, *J. Environ. Chem. Eng.*, 2025, **13**, 118127.
9 S. Wang, D. Wang, G. Wang, M. Zhang, Y. Sun and J. Ding, *Mater. Today Bio*, 2025, **30**, 101383.
10 P. Feng, R. He, F. Yang, Y. Lin, L. Fan, H. Pan and C. Shuai, *Sustainable Mater. Technol.*, 2025, **43**, e01205.
11 V. Khwaza and B. A. Aderibigbe, *Antibiotics*, 2025, **14**, 68.
12 Z. Zhang, M. Cao, Z. Shang, J. Xu, X. Chen, Z. Zhu, W. Wang, X. Wei, X. Zhou, Y. Bai and J. Zhang, *Antibiotics*, 2025, **14**, 334.
13 J. Fu, C. Wang, X. Liu, S. Zhu, Y. Zheng, Z. Li, Z. Cui, Y. Zhang, H. Jiang, Y. Cao, P. K. Chu and S. Wu, *Prog. Mater. Sci.*, 2026, **155**, 101532.
14 L. L. Silver, *Clin. Microbiol. Rev.*, 2011, **24**, 71–109.
15 R. D. Süssmuth, M. Kulike-Koczula, P. Gao and S. Kosol, *Angew. Chem., Int. Ed.*, 2025, **64**, e202414325.
16 G. A. Niño-Vega, J. A. Ortiz-Ramírez and E. López-Romero, *Antibiotics*, 2025, **14**, 404.
17 J. Yang and Y. Yang, *Small*, 2020, **16**, 1906846.
18 P. Sezgin, E. Gulcay-Ozcan, M. Vučkovski, A. M. Bondžić, I. Erucar and S. Keskin, *Ind. Eng. Chem. Res.*, 2025, **64**, 1907–1932.
19 V. Shukla and K. A. Siddiqui, *CrystEngComm*, 2025, **27**, 4443–4452.
20 S. Zarei-Shokat, S. Abedi-Banaei, A. Kashtiaray, Z. Yazdi, H. Amirhosseini and A. Maleki, *Mater. Adv.*, 2025, **6**, 4174–4196.
21 B. Thanh Le, C. Que Nguyen, H. Duc Ninh, P. Thi Nguyen, D. Duc La and H. Phuong Nguyen Thi, *ChemistrySelect*, 2024, **9**, e202402854.
22 B. T. Le, D. D. La and P. T. H. Nguyen, *ACS Omega*, 2023, **8**, 1262–1270.
23 B. T. Le, C. Q. Nguyen, P. T. Nguyen, H. D. Ninh, T. M. Le, P. T. H. Nguyen and D. D. La, *ACS Omega*, 2022, **7**, 46674–46681.
24 P. T. H. Nguyen, B. T. Le, H. D. Ninh and D. D. La, *ACS Omega*, 2021, **6**, 33419–33427.
25 G. T. Tran, T. T. T. Nguyen and T. Van Tran, *Coord. Chem. Rev.*, 2025, **544**, 217002.
26 P. Borah, S. Roy and M. Ahmaruzzaman, *Adv. Colloid Interface Sci.*, 2025, **344**, 103613.
27 Z. Yu, M. Lepoitevin and C. Serre, *Adv. Healthcare Mater.*, 2025, **14**, 2402630.
28 A. Zuliani, V. Ramos, A. Escudero and N. Khiar, *Nanoscale Horiz.*, 2025, **10**, 258–278.

29 M. Abbas, Z. Liang, M. Chen, W. Qu, S. Khan, M. S. Ashaq, D. Chen and S. Xie, *Biol. Trace Elem. Res.*, 2025, **204**, 836–852.
30 Z. Yu, A. Chivu, J. Dai, H. K. Patra, J. Zou and Z. Hu, *Coord. Chem. Rev.*, 2026, **549**, 217262.
31 D. K. Chandra, A. Kumar and C. Mahapatra, *Hybrid Adv.*, 2025, **9**, 100406.
32 T. Zhang, Y. Yu, Y. Lu, H. Tang, K. Chen, J. Shi, Z. Ren, S. Wu, D. Xia and Y. Zheng, *Prog. Mater. Sci.*, 2026, **155**, 101526.
33 P. K. Samantaray, S. Baloda, G. Madras and S. Bose, *J. Mater. Chem. A*, 2018, **6**, 16664–16679.
34 Z. Deng, M. Li, Y. Hu, Y. He, B. Tao, Z. Yuan, R. Wang, M. Chen, Z. Luo and K. Cai, *Chem. Eng. J.*, 2021, **420**, 129668.
35 C. Guo, F. Cheng, G. Liang, S. Zhang, Q. Jia, L. He, S. Duan, Y. Fu, Z. Zhang and M. Du, *Chem. Eng. J.*, 2022, **435**, 134915.
36 J. Wen, Y. Guo, X. Li, B. Wang, H. Wang, X. Gao, B. Niu and W. Li, *Food Biosci.*, 2024, **61**, 104959.
37 S. Zhou, J. Zhu, Z. Wang, Z. Yang, W. Yang and Z. Yin, *Water Res.*, 2022, **220**, 118635.
38 L. Liao, R. Yuan, Z. Li and W. Zhou, *Adv. Colloid Interface Sci.*, 2025, **341**, 103485.
39 G. Lin and U. Mirsaidov, *Adv. Sci.*, 2025, **12**, 2500984.
40 K. Kumari, G. Mishra and S. K. Singh, *Inorg. Chem.*, 2025, **64**, 18254–18264.
41 Z. Wang, H. Meng, X. Liu, N. Wu, L. Yang, B. Wu, G. Li, Q. Liu, J. Li, J. Ge and C. Wang, *Chem. Eng. J.*, 2025, **521**, 166299.
42 H. Li, Z. Xiao, R. Hao, X. Tan, F. Ye, J. Gu, J. Li, G. Li, J.-J. Zou and D. Wang, *Sep. Purif. Technol.*, 2025, **365**, 132637.
43 H. Yu, D. Chen, X. Wang, L. Yang, G. Wang and P. Hu, *Acta Phys.-Chim. Sin.*, 2025, 100201.
44 W. Fan, Z. Yu, D. Appadoo, K. Liang and J. Liang, *Small*, 2025, **21**, 2503059.
45 X. Wang, H. Xu, Q. Wang, J. Ma, M. Lin, L. Zhou, M. Wu, G. Hao, Y. Du, A. Li, Y. An, X. Zhang, W. Chang, I. Chen, H. Lu, J. Li, H. G. Tsai, H. Liu, F. Shieh and L. Chou, *Angew. Chem.*, 2025, **64**, e202509275.
46 H. N. Abdelhamid, M. Dowaidar and Ü. Langel, *Microporous Mesoporous Mater.*, 2020, **302**, 110200.
47 H. N. Abdelhamid, Z. Huang, A. M. El-Zohry, H. Zheng and X. Zou, *Inorg. Chem.*, 2017, **56**, 9139–9146.
48 H. N. Abdelhamid, *J. Environ. Chem. Eng.*, 2020, **8**, 104008.
49 H. N. Abdelhamid, *Macromol. Chem. Phys.*, 2020, **221**, 2000031.
50 Q. Wu, J. Liang, D. Wang, R. Wang and C. Janiak, *Chem. Soc. Rev.*, 2025, **54**, 601–622.
51 N. Ma, K. Cai, J. Zhao, C. Liu, H. Li, P. Tan, Y. Li, D. Li and X. Ma, *Adv. Mater.*, 2025, **37**, 2503056.
52 M. Ishfaq, D. Lateef, Z. Ashraf, M. Sajjad, M. Owais, W. Shoukat, M. Mohsin, M. Ibrahim, F. Verpoort and A. H. Chughtai, *RSC Adv.*, 2025, **15**, 26647–26659.
53 H. N. Abdelhamid and X. Zou, *Green Chem.*, 2018, **20**, 1074–1084.
54 F.-X. Wang, I. Prokes, L. Song, H. Shi and P. J. Sadler, *JBIC, J. Biol. Inorg. Chem.*, 2022, **27**, 695–704.
55 S. S. Abdel-Hakeem, G. A.-E. Mahmoud and H. H. Abdel-Hafeez, *Microsc. Microanal.*, 2019, **25**, 1498–1508.
56 G. Abd-Elmonsef Mahmoud, Y. A. Osman and S. S. Abdel-Hakeem, *Microb. Pathog.*, 2020, **147**, 104404.
57 V. Kuete, S. Alibert-Franco, K. O. Eyong, B. Ngameni, G. N. Folefoc, J. R. Nguemeving, J. G. Tangmouo, G. W. Fotso, J. Komguem, B. M. W. Ouahouo, J.-M. Bolla, J. Chevalier, B. T. Ngadjui, A. E. Nkengfack and J.-M. Pagès, *Int. J. Antimicrob. Agents*, 2011, **37**, 156–161.
58 J. M. Andrews, *J. Antimicrob. Chemother.*, 2001, **48**, 5–16.
59 H. Nasser Abdelhamid, S. Sultan and A. P. Mathew, *Chem. Eng. J.*, 2023, **468**, 143567.
60 H. N. Abdelhamid, *Dalton Trans.*, 2023, **52**, 2506–2517.
61 H. Nasser Abdelhamid and A. P. Mathew, *Chem. Eng. J.*, 2021, **426**, 131733.
62 Z. Ren, W. Zhang, J. Li, S. Wang, J. Liu and Y. Lv, *J. Chem. Eng. Data*, 2010, **55**, 2687–2694.
63 M. A. Hossain, M. Friciu, S. Aubin and G. Leclair, *Am. J. Heal. Pharm.*, 2014, **71**, 669–673.
64 J. Qi, Q. Liu and H. Liu, *Chin. J. Chem. Eng.*, 2018, **26**, 1430–1434.
65 X. Lu, H. Xing, B. Su and Q. Ren, *J. Chem. Eng. Data*, 2008, **53**, 543–547.
66 H. N. Abdelhamid, *Curr. Med. Chem.*, 2021, **28**, 7023–7075.
67 H. N. Abdelhamid, T. H. Taha, A. M. Alhudhaibi and A. K. Saleh, *Int. J. Biol. Macromol.*, 2025, **334**, 149040.
68 H. Nasser Abdelhamid, *Eur. Cell. Mater.*, 2025, DOI: 10.22203/eCM.v054a07.
69 F. E. A. Abd El-Aziz and H. N. Abdelhamid, *Appl. Organomet. Chem.*, 2024, **38**, e7520.
70 H. N. Abdelhamid and W. Sharmoukh, *Microchem. J.*, 2021, **163**, 105873.
71 A. I. A. Soliman, A. M. A. Abdel-Wahab and H. N. Abdelhamid, *RSC Adv.*, 2022, **12**, 7075–7084.
72 C. Ou, F. Yang, M. Gong, C. Xu, S. Yang, J. Yang, W. Qi, Y. Luo, Z. Peng, L. Deng and D. He, *ACS Appl. Nano Mater.*, 2023, **6**, 15860–15870.
73 P. Li, J. Li, X. Feng, J. Li, Y. Hao, J. Zhang, H. Wang, A. Yin, J. Zhou, X. Ma and B. Wang, *Nat. Commun.*, 2019, **10**, 2177.
74 S. Zhang, J. Ye, X. Liu, Y. Wang, C. Li, J. Fang, B. Chang, Y. Qi, Y. Li and G. Ning, *J. Colloid Interface Sci.*, 2021, **599**, 390–403.
75 R. Antwi-Baah, M. E. E. Acquah, M. F. Dapaah, Y. Wang, X. Chen, J. Walker and H. Liu, *Colloids Surf., A*, 2025, **706**, 135768.
76 Y. Tu, C. Lei, F. Deng, Y. Chen, Y. Wang and Z. Zhang, *New J. Chem.*, 2021, **45**, 8701–8713.
77 Q. Qiu and L. Lan, *Cellulose*, 2025, **32**, 2663–2678.
78 T. Liu, A. Zhang, M. Zhou, Y. Wang, S. Xie and Z.-X. Lu, *New J. Chem.*, 2023, **47**, 3825–3833.
79 M. Rahman, M. Kabir, T. Islam, Y. Wang, Q. Meng, H. Liu, S. Chen and S. Wu, *ACS Omega*, 2025, **10**, 3067–3079.
80 Z. Yu, Y. Shi, J. Lin, Y. Wang, C. He and J. Cheng, *Int. J. Biol. Macromol.*, 2025, **319**, 145130.
81 H. N. Abdelhamid, *Biointerface Res. Appl. Chem.*, 2021, **11**, 8283–8297.
82 H. N. Abdelhamid and F. E.-Z. A. Abd El-Aziz, *New J. Chem.*, 2025, **49**, 11218–11226.